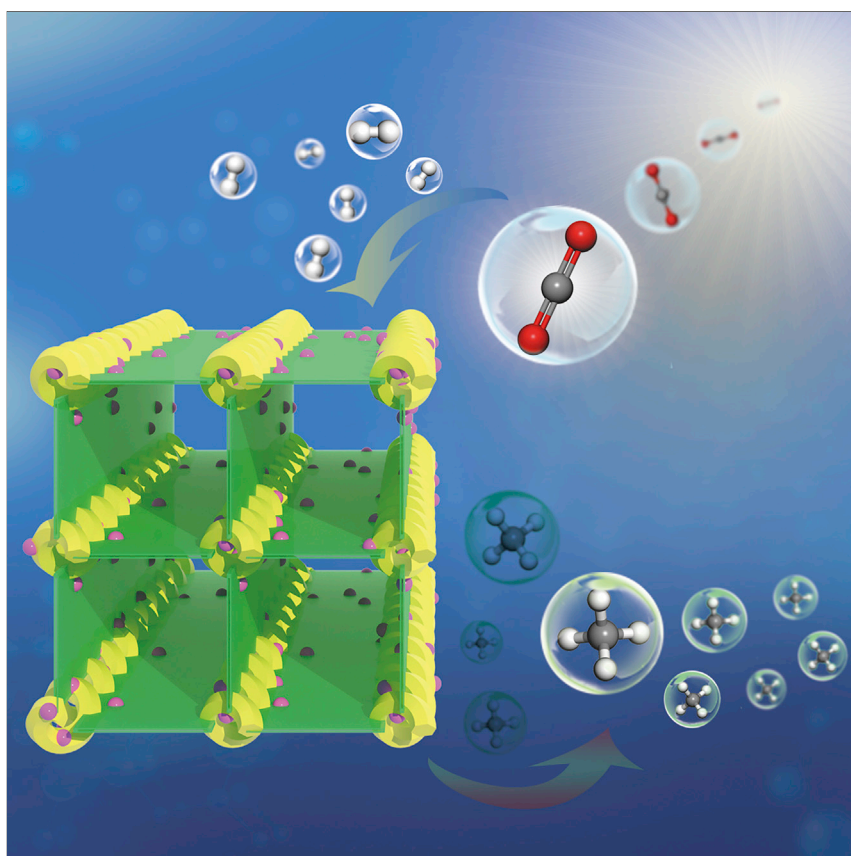


## Article

# A Robust Titanium Isophthalate Metal-Organic Framework for Visible-Light Photocatalytic CO<sub>2</sub> Methanation



MIP-208, which is constructed from Ti–O helical chain and isophthalate derivative linker, was obtained with a high crystallinity through *in situ* transformation of inorganic and organic precursors. Its good stability and tunable porosity, once combined with RuO<sub>x</sub> nanoparticles, was exploited for the photocatalytic methanation of CO<sub>2</sub> under visible light, reaching a high and durable productivity of 0.8 mmol g<sub>catalyst</sub><sup>-1</sup> at 200°C in 22 h.

Sujing Wang, Maria  
Cabrero-Antonino, Sergio  
Navalón, ..., William Shepard,  
Hermenegildo García, Christian  
Serre

sjwang4@ustc.edu.cn (S.W.)  
hgarcia@qim.upv.es (H.G.)  
christian.serre@ens.fr (C.S.)

## HIGHLIGHTS

Ti-MOF based on Ti–O helical chain and feedstock isophthalate linker is achieved

*In situ* transformation of reaction precursors significantly tunes the reaction rate

MIP-208 features good stability and tunable porosity

MIP-208@RuO<sub>x</sub> shows an efficient visible-light photocatalytic methanation of CO<sub>2</sub>

Article

# A Robust Titanium Isophthalate Metal-Organic Framework for Visible-Light Photocatalytic CO<sub>2</sub> Methanation

Sujing Wang,<sup>1,2,8,\*</sup> Maria Cabrero-Antonino,<sup>3</sup> Sergio Navalón,<sup>3</sup> Chen-chen Cao,<sup>1</sup> Antoine Tissot,<sup>1</sup> Iurii Dovgaluk,<sup>1</sup> Jérôme Marrot,<sup>4</sup> Charlotte Martineau-Corcos,<sup>4,5</sup> Liang Yu,<sup>6</sup> Hao Wang,<sup>6</sup> William Shepard,<sup>7</sup> Hermenegildo García,<sup>3,\*</sup> and Christian Serre<sup>1,\*</sup>

## SUMMARY

**Isophthalic acid (IPA) has been considered to build metal-organic frameworks (MOFs), owing to its facile availability, unique connection angle-mode, and a wide range of functional groups attached. Constructing titanium-IPA frameworks that possess photoresponse properties is an alluring characteristic with respect to the challenge of synthesizing new titanium-based MOFs (Ti-MOFs). Here, we report the first Ti-IPA MOF (MIP-208) that efficiently combines the use of preformed Ti<sub>8</sub> oxoclusters and *in situ* acetylation of the 5-NH<sub>2</sub>-IPA linker. The mixed solid-solution linkers strategy was successfully applied, resulting in a series of multivariate MIP-208 structures with tunable chemical environments and sizable porosity. MIP-208 shows the best result among the pure MOF catalysts for the photocatalytic methanation of carbon dioxide. To improve the photocatalytic performance, ruthenium oxide nanoparticles were photo-deposited on MIP-208, forming a highly active and selective composite catalyst, MIP-208@RuO<sub>x</sub>, which features a notable visible-light response coupled with excellent stability and recycling ability.**

## INTRODUCTION

Metal-organic frameworks (MOFs) or porous coordination polymers have been recognized as one of the most intensively investigated heterogeneous catalysts for liquid-phase reactions due to their porous tunable structure, high surface area, and acidic-basic sites or metal nodes with versatile and spatially controlled distributions.<sup>1–3</sup> Organic ligands play an essential role in the formation of the MOF structure and the introduction of its corresponding property.<sup>4,5</sup> As organic synthesis has evolved significantly over the last few decades, an almost unlimited number of organic compounds have been applied to MOF fabrication via the linker engineering strategy, resulting in a vast combination of structures and functions.<sup>6–9</sup> However, the time and effort requiring organic synthesis for linker preparation undoubtedly limits the reproduction and application of costly MOF candidates.<sup>10,11</sup> In this regard, commercially available organic linkers from the industry are of great interest due to their ready availability on a large scale and low cost.<sup>12,13</sup>

Benzene-dicarboxylic acid isomers are representative compounds that fulfill the aforementioned demand currently produced on a billion-kilogram scale per annum. The three isomers, namely *ortho*-phthalic acid (phthalic acid), *meta*-phthalic acid

## The Bigger Picture

The photocatalytic methanation of CO<sub>2</sub> is challenging for metal-organic-framework (MOF)-based materials due to the necessary combination of good hydrolytic stability, good photoresponsive properties, and optimal CO<sub>2</sub> sorption character at high temperatures. Titanium-based MOFs (Ti-MOFs) are promising candidates for such a demanding reaction, but state-of-the-art Ti-MOFs exhibit limited chemical stability and often show poor photophysical properties, which makes them incompatible for CO<sub>2</sub> methanation.

We report a Ti-MOF photocatalyst (MIP-208), based on Ti-O helical chains and isophthalate linker, that not only displays an outstanding stability but also possesses the best CO<sub>2</sub> methanation performance for a bare MOF. A significantly enhanced photocatalytic activity can be achieved by the deposition of a RuO<sub>x</sub> co-catalyst. These results illustrate the continuous interest in the synthesis of novel robust photoactive Ti-MOFs to develop new generations of sustainable photocatalysts, suitable for the production of solar fuels and the utilization of CO<sub>2</sub>.

(isophthalic acid, IPA), and *para*-phthalic acid (terephthalic acid), are all important feedstocks for the preparation of a large number of industrial products.<sup>14,15</sup> With respect to their use in constructing MOFs, phthalic acid alone tends to form materials of low dimensionality, mainly due to the deficient separation and steric hindrance between the adjacent carboxylate groups.<sup>16,17</sup> On the contrary, terephthalic acid is one of the most popular carboxylate linkers since the very beginning of MOF science.<sup>18</sup> Its ideal configuration with a suitable molecular length, perfect separation of the coordination sites, and varied connection modes, make this linker adaptable to MOF structures with any dimension and built with almost every type of metal element.<sup>19–21</sup>

In the case of IPA, the unique angle (120°) and the medium distance between the two carboxylate groups enable a large degree of manipulation in the synthesis of MOFs compared with the other two isomers. Numerous metal-IPA frameworks have been identified with nodes ranging from the alkaline earth metals,<sup>22</sup> to divalent and trivalent transition metals,<sup>23–26</sup> as well as rare earth<sup>27–29</sup> or main group elements,<sup>30–32</sup> and even mixed metal systems,<sup>33–35</sup> in which the meta side of the coordinated carboxylate groups on the benzene ring frequently faces the structure void. Thus, IPA offers an obvious and facile opportunity of tuning the chemical environment of the MOF pore via the introduction of functional groups on the meta side. Correspondingly, distinct organic functions on the 5- and 4-position of the benzene ring have been reported, invoking great interest and showing potential in terms of fine-tuning the structure-property correlation.<sup>36–39</sup>

It is noteworthy that IPA is suitable for MOF assembly with every transition metal subgroup except for the group 4 elements in the periodic table, and to the best of our knowledge, there has been no report of IPA-based-MOF examples built with titanium (Ti), zirconium (Zr), hafnium (Hf), or rutherfordium (Rf). However, Ti and Zr, the most common group 4 metals, have attracted much attention from the MOF research community during the past years due to their high natural abundance, low toxicity, and strong interactions with oxygen sites and thus significantly enhanced stabilities once in the MOF structures.<sup>40,41</sup>

More recently, the potential of MOFs has expanded into other areas of catalysis, particularly in photocatalysis.<sup>42</sup> The strong interaction between the positively charged metal nodes and negatively charged antenna linkers in rigid configurations makes MOFs suitable for the promotion of photoinduced charge separation.<sup>42</sup> Hence, an electron transfer from the organic linker in its excited state to the metal node upon light absorption appears to be a general photochemical step, especially in the case of a favorable overlap between the lowest occupied crystal orbital with the atomic orbitals of the metal cations.<sup>43</sup> For this reason, MOFs are among the most promising categories of porous photocatalysts, particularly for the production of solar fuels.

Taking into account the prevalent role of MOFs and derivative materials in photocatalysis, Ti-MOFs have attracted considerable attention due to the known activities of TiO<sub>2</sub> and Ti-oxo clusters to undergo photoinduced charge separation.<sup>44</sup> In general, Ti-MOFs are not only considered promising candidates as photo-responsive materials<sup>45</sup> but also show great potential in gas separation,<sup>46,47</sup> proton conduction,<sup>48</sup> and clinical applications.<sup>49</sup> Nevertheless, the direct synthesis of Ti-MOFs still remains an important challenge,<sup>50</sup> despite the gradually increasing numbers of reported Ti-MOF structures over the past decade, which have been attained mostly through serendipity. It is expected that an infinite number of interconnected Ti-O

<sup>1</sup>Institut des Matériaux Poreux de Paris, Ecole Normale Supérieure, ESPCI Paris, CNRS, PSL Université, 75005 Paris, France

<sup>2</sup>CAS Key Laboratory of Microscale Magnetic Resonance, Hefei National Laboratory for Physical Sciences at the Microscale, University of Science and Technology of China, Hefei 230026, Anhui, China

<sup>3</sup>Departamento de Química and Instituto de Tecnología Química (ITQ), CSIC-UPV), Universitat Politècnica de València, 46022 Valencia, Spain

<sup>4</sup>Institut Lavoisier de Versailles, UMR 8180 CNRS, Université de Versailles – Saint-Quentin-En-Yvelines, Université Paris-Saclay, 78035 Versailles, France

<sup>5</sup>CEMHTI, UPR 3079 CNRS, 45071 Orléans Cedex 2, France

<sup>6</sup>Hoffmann Institute of Advanced Materials, Shenzhen Polytechnic, Shenzhen 518055, Guangdong, China

<sup>7</sup>Synchrotron SOLEIL, L'Orme des Merisiers, Saint-Aubin, BP 48, 91192 Gif-sur-Yvette, France

<sup>8</sup>Lead Contact

\*Correspondence: [sjwang4@ustc.edu.cn](mailto:sjwang4@ustc.edu.cn) (S.W.), [hgarcia@qim.upv.es](mailto:hgarcia@qim.upv.es) (H.G.), [christian.serre@ens.fr](mailto:christian.serre@ens.fr) (C.S.)

<https://doi.org/10.1016/j.chempr.2020.10.017>

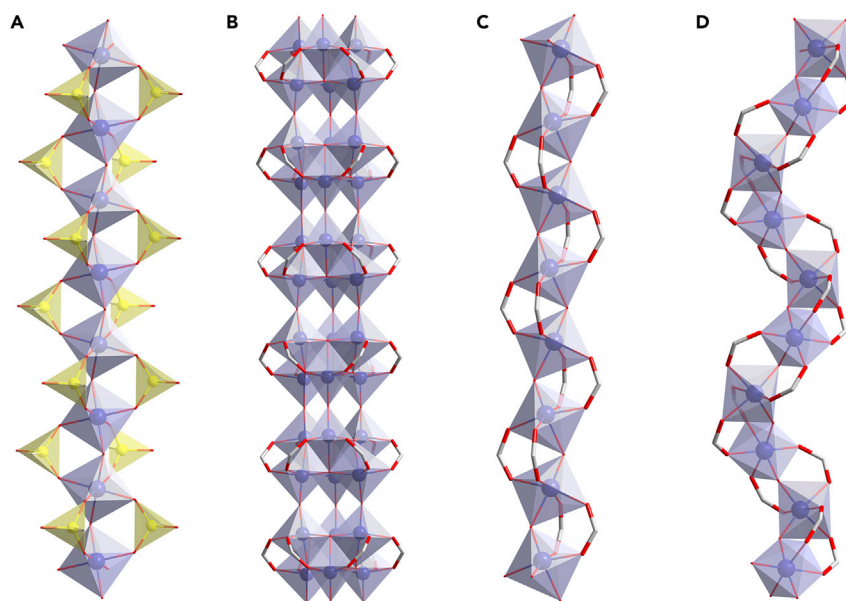


**Figure 1. Comparison of 1D Ti-O Inorganic Building Units Reported**

- (A) Linear TiO chain in MIL-91.  
(B) Linear Ti<sub>6</sub>O<sub>9</sub> nanowire in MIP-177-HT and ZSTU-1, 2, and 3.  
(C) Linear TiO chain in DGIST-1 and ACM-1.  
(D) Helical TiO chain in MIP-208 reported here.

units would facilitate photoinduced charge separation and charge mobility, in comparison with MOFs based on discrete inorganic units with a low number of Ti–O bonds. Thus, one and two-dimensional (1D and 2D) arrays of Ti–O units should in principle improve the semiconducting properties of the Ti-MOFs.<sup>51</sup> In this context, the photoactive Ti-MOFs that have been prepared thus far are those with 1D chains or nanowires of Ti–O building units, whose photo-responsive behavior has been proven to be closer to those of bulk Ti–O than the compounds constructed of discrete TiO<sub>2</sub>.<sup>52</sup> As shown in Figure 1, there are only three kinds of 1D Ti–O inorganic building units reported to date, namely the TiO chains in MIL-91<sup>53</sup>; the Ti<sub>6</sub>O<sub>9</sub> nanowires in MIP-177-HT<sup>52</sup> and ZSTU-1, 2, and 3<sup>54</sup>; and the TiO chain in DGIST-1.<sup>55</sup> Therefore, as these MOFs are all constructed from sophisticated ligands, it would be of great interest to synthesize IPA-type linker-based Ti-MOFs with infinite Ti–O building units. It would expand the scope of the structural and chemical diversity of Ti-MOFs and may also lead to improved photocatalytic performances.

Herein, we report an ultramicroporous Ti-MOF, denoted as MIP-208 (MIP stands for the Materials of the Institute of Porous Materials from Paris), the first MOF composed of group 4 metal and IPA-type linker. In the crystal structure of MIP-208, helical chains of *cis*-connected corner-sharing TiO<sub>6</sub> polyhedra are held in place by the *in-situ*-generated 5-acetamidoisophthalate (5-Aa-IPA) linker molecules, giving rise to a 3D framework with 1D-channel-like accessible voids running along the c axis. Benefiting from their shared structural configuration and coordination adaptability, mixed linkers of 5-Aa-IPA and other IPA derivatives with diverse functional groups on the meta position of the carboxylate groups could be further introduced in the framework following the use of a solid-solution strategy, resulting in a series of multivariate MIP-208 structures. Furthermore, the dual presence of the amide group and the 1D TiO chain unit in the porous structure of MIP-208, associated with an excellent thermal and hydrothermal stability, has allowed the development of a photocatalyst

for the methanation of carbon dioxide (CO<sub>2</sub>) based on RuO<sub>x</sub> nanoparticles (NPs) under visible light, reaching a productivity of 0.8 mmol g<sub>catalyst</sub><sup>-1</sup> at 200°C in 22 h.

## RESULTS AND DISCUSSION

Twenty-four different Ti-MOFs prepared from direct synthesis have been reported to date. The Ti sources used to produce these MOFs can be classified into two types: simple Ti complexes and polynuclear TiO clusters. Compared with simple Ti complexes, such as TiCl<sub>3</sub>, TiCl<sub>4</sub>, and Ti(iPrO)<sub>4</sub>, Ti-oxoclusters are known to slow down the reaction rate and avoid the undesirable hydrolytic formation of TiO<sub>2</sub> owing to the gradual rearrangements of Ti–O connections of the oxo cluster precursor for most cases. Thus, Ti-oxoclusters usually lead to highly crystalline Ti-MOF materials composed of large single crystals.<sup>55–57</sup> In this regard, a Ti<sub>8</sub>O<sub>8</sub> cluster with formate and acetate terminals (Ti<sub>8</sub>AF) was selected here as a reactant due to its facile preparation and easy handling coupled with suitable stability and reactivity.<sup>58</sup> Regarding solvent for the reaction, it is well recognized that the conventional ones, such as dimethylformamide (DMF) and diethylformamide, should be replaced by greener solvents to decrease the toxicity to humans and the environment. Based on our previous success of preparing group 4 metal MOFs, formic acid, acetic acid and acetic anhydride, which have been shown to efficiently slow down the reaction leading to highly crystalline products, were selected as solvents. 5-NH<sub>2</sub>-IPA was selected as the linker due to the documented benefit of the amino group presence in increasing the CO<sub>2</sub> adsorption and enhancing the visible-light photoresponse.<sup>59,60</sup>

Initial reaction attempts indicated that the aforementioned three acidic solvents can interfere with the decomposition of the Ti<sub>8</sub>AF precursor while offering a good solubility for the 5-NH<sub>2</sub>-IPA linker. However, all attempts did not generate any crystalline solid. Various additives known to either facilitate the linker exchange or promote the rearrangement of Ti–O connections were tested, such as water, methanol, ethanol, acetone, and DMF. A highly crystalline product of a dark yellow or light brown color was formed only when methanol was used in the mixture of acetic acid and acetic anhydride. Acetic acid was found to be not necessary for the product formation, but to accelerate the reaction rate. An *in situ* amidation took place between the amino group of 5-NH<sub>2</sub>-IPA and acetic anhydride, generating the 5-acetamide-IPA (5-Aa-IPA) as the final framework building linker (Figure S1). Solid-state NMR data collected on the as-synthesized MIP-208 sample demonstrated the complete conversion of 5-NH<sub>2</sub>-IPA to 5-Aa-IPA, which serves as the linker to build the MOF structure (Figures S2–S4).

It is likely that the *in situ* acetylation step is critical to yield the crystalline material, which possibly slows down the reaction rate significantly. A control experiment using the preformed 5-Aa-IPA as linker under the same reaction conditions did not lead to MIP-208, but to an amorphous solid. Therefore, this solvothermal synthesis is likely to benefit synergistically from the rearrangement of the Ti<sub>8</sub>AF cluster and *in situ* linker formation, which is a rare case for MOF preparation reported thus far. However, it could provide a valuable and even rational strategy for the synthesis of new Ti-MOFs through a control of the reaction rate from both inorganic and organic precursor conversions.

MIP-208 was obtained as micro-sized single crystals, ruling out its structure determination from laboratory diffraction. Thus single-crystal X-ray diffraction data of MIP-208 were collected with micro-focused X-rays on the synchrotron beamline PPOXIMA 2A (Synchrotron SOLEIL, France)<sup>61</sup> to determine its crystal structure.

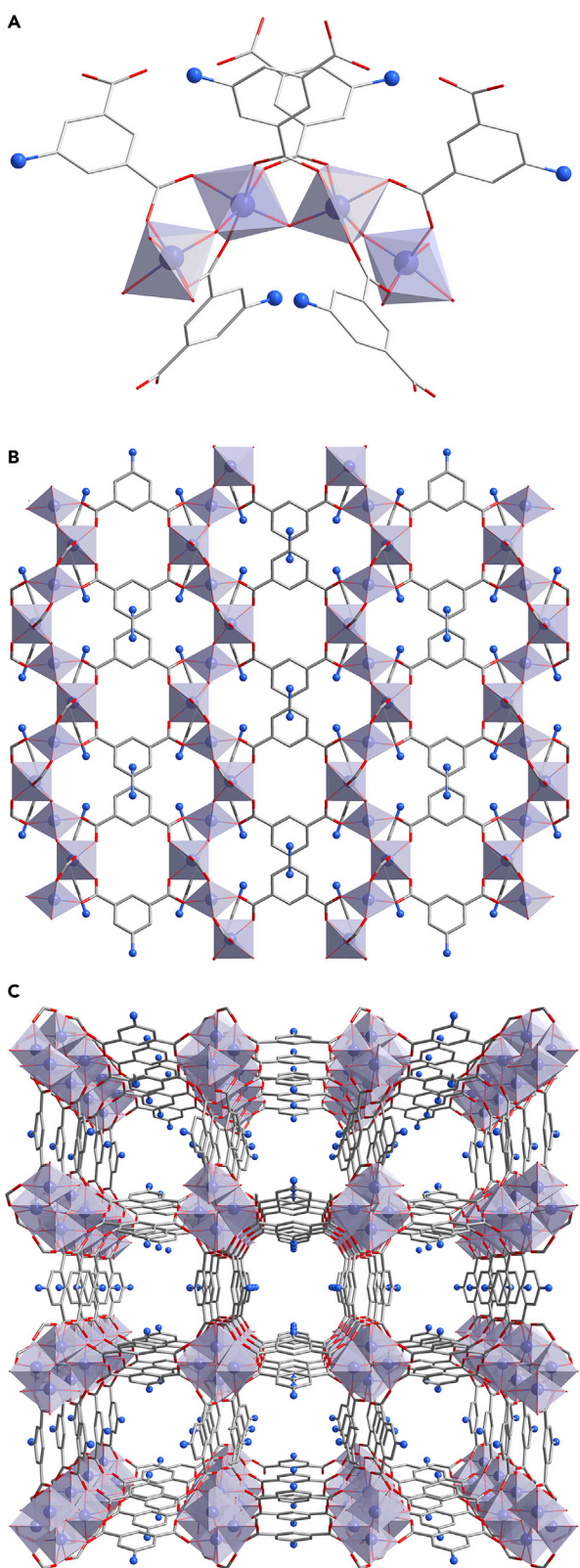


**Figure 2. Crystal Structure of MIP-208**

- (A) Coordination environment of the Ti<sup>4+</sup> ions and arrangement of 5-Aa-IPA linkers around them.
- (B) Structure viewed along the b axis.
- (C) Structure viewed along the c axis, showing 1D channels (Ti in purple, C in gray, and O in red; the blue ball represents the acetamide group. All hydrogen atoms are omitted for clarity).

The coordination environment of the Ti<sup>4+</sup> ion and the overall framework connection could be solved precisely, even though the position of the acetamide group could not be accurately located due to its disorder. Assisted by the solid-state NMR characterization, an empirical formula of Ti( $\mu_2$ -O)(5-Aa-IPA) could be determined for MIP-208. Rietveld refinement carried out on the high-resolution powder X-ray diffraction data (PXRD) of MIP-208 confirms the aforementioned structural model (Figure S5). It crystallizes in tetragonal  $I4_1/AMD$  space group (no. 141) with the unit-cell constants  $a = b = 21.8190 \text{ \AA}$  and  $c = 10.9380 \text{ \AA}$ . As shown in Figure 2A, each Ti<sup>4+</sup> ion is in an octahedral coordination geometry with four carboxylate oxygen atoms and two  $\mu_2$ -O oxo groups. The adjacent TiO<sub>6</sub> polyhedra adopt a *cis*-connected corner-sharing mode to connect each other, giving rise to a 1D infinite chain of secondary building units (SBUs) running along the c axis. Unlike the linear 1D Ti-O SBUs in MIL-91,<sup>53</sup> DGIST-1,<sup>55</sup> and MIP-177-HT,<sup>52</sup> to our knowledge, the helical TiO chain in MIP-208 is the first example of this type of SBU observed in Ti-MOFs (Figure 1). An Al(OH) chain with a similar configuration was discovered previously in the CAU-10 MOF series (CAU stands for Christian-Albrechts-University),<sup>62</sup> with  $\mu_2$ -OH group as the shared corner.

Of note, the replacement of the bridging OH in trivalent metal-based MOFs by an oxo group in similar MOFs built with tetravalent metals could lead to a dramatic difference in terms of structural flexibility and related properties, as documented in MIL-47 and MIL-53 compounds (MIL stands for Materials from Institute Lavoisier).<sup>63,64</sup> In particular, the presence of OH or oxo groups in Ti-O materials has been demonstrated to be critical to their performance in photocatalysis,<sup>65–67</sup> which highlights the importance of TiO chains in MIP-208 structure over its analogs with the lower valence metal ions.

The neighboring TiO chains are interconnected via pairs of 5-Aa-IPA linkers in an up-and-down mode to avoid as much as possible any steric hindrance (Figure 2B), resulting in a 3D framework with double-walled 1D channels running along the c axis (Figure 2C). One can expect its micropores to be accessible for guest molecules as reported before for CAU-10 compounds constructed from IPA bearing the bulkiest functional groups<sup>62,68</sup> due to the large size and thus considerable steric hindrance of the acetamide groups facing the pores. As reported before for CAU-10-OMe and CAU-10-Br, MIP-208 did not show any accessibility for nitrogen at 77 K, but a noticeable porosity for CO<sub>2</sub> (Figure S4).

A large number of functionalized IPAs are commercially available chemicals offered at low prices. The high compatibility of IPA derivatives regarding their behavior in coordination chemistry has been documented,<sup>37</sup> thus offering the possibility to tune the chemical environment of the pore in the MIP-208 structure via a solid-solution mixed linker strategy. The solid-solution synthesis strategy is a powerful alternative way to introduce multiple functional groups together in MOF structures, especially when the direct synthesis of the isostructural MOF with the single linker bearing specific functional group as a reactant is challenging.<sup>69–71</sup> This strategy suits perfectly the case of MIP-208 because all attempts to directly synthesize the corresponding MIP-208 analogs using other functionalized IPAs instead of 5-NH<sub>2</sub>-IPA have failed thus far, resulting in either amorphous solids or crystalline phases of different structures.

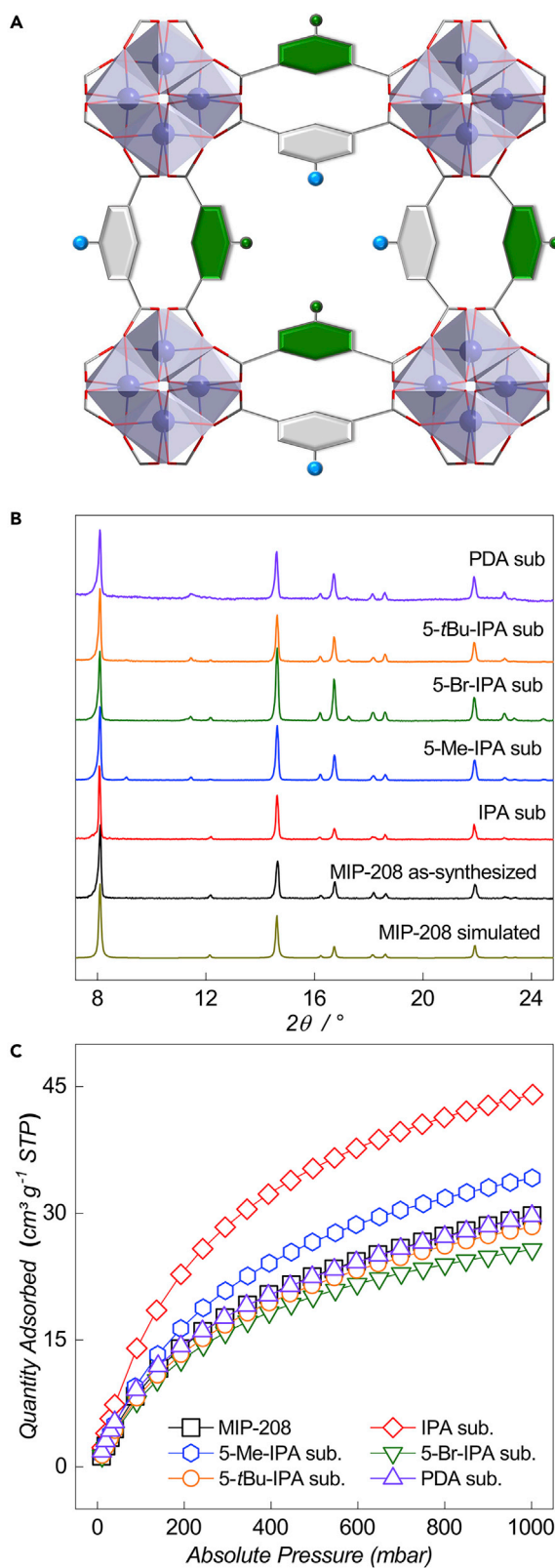


**Figure 3. Illustration and Characterizations of MTV-MIP-208 Materials**

(A) Illustration of MTV-MIP-208 structure with multiple functional groups (the blue ball represents the acetamide group, and the green ball represents the other functional groups. Hydrogen atoms are omitted for clarity).

(B) PXRD patterns of the parent and MTV-MIP-208s ( $\lambda_{\text{Cu}} \approx 1.5406 \text{ \AA}$ ).

(C) CO<sub>2</sub> adsorption isotherms collected at 273 K for parent and MTV-MIP-208 solids.

Therefore, mixed linkers were considered via one-pot reactions to prepare a series of multivariate MIP-208s (MTV-MIP-208, Figure 3A). Several representative IPA-type dicarboxylic acids, including IPA, 5-NO<sub>2</sub>-IPA, 5-Me-IPA, 5-Br-IPA, 5-tBu-IPA, 3,5-pyrazole-dicarboxylic acid (PDA), and camphoric acid, were selected as the substitution linkers, aiming to replace the 5-Aa-IPA spacer in the MIP-208 framework. All the tested linkers except 5-NO<sub>2</sub>-IPA and camphoric acid could reach certain substitution ratios, ranging from 11 to 50 mol % (Figure S8), as deduced from the NMR data. However, the reason for the unsuccessful inclusion of 5-NO<sub>2</sub>-IPA and camphoric acid is not yet clear and still under investigation.

As shown in Figure 3B, the inclusion of the second linker did not generate noticeable changes in the overall structural long-range order, as evidenced by their highly similar PXRD patterns. However, the porosities of the resulting materials were altered, as deduced from the CO<sub>2</sub> adsorption isotherms collected at 273 K (Figure 3C). For instance, the sample with 50 mol % IPA substitution ratio led to a significant enhancement of CO<sub>2</sub> uptake (50% at both 0.15 and 1 bar) compared with the pure MIP-208, likely because of the smaller H atoms providing less steric hindrance over the larger acetamide group. A similar observation was noticed for the 5-Me-IPA mixed sample (33 mol %). In the case of the 5-Br-IPA derivative (38 mol %), a slight decrease of uptake in comparison with the parent compound was observed, possibly attributable to the much heavier atomic weight of the Br atom, despite its lower steric hindrance. When the slightly bulkier tBu group, but of similar molecular weight, was introduced to replace the acetamide group, the sample showed a limited drop in pore volume mainly due to the small linker substitution ratio (17 mol %). It is worth noting that even PDA, which has a five-membered heterocyclic aromatic moiety, could be included in the MIP-208 framework, though the substitution ratio was low (11 mol %), probably due to the small change in the angle of the two carboxylate groups and the presence of basic N-site on the heterocyclic ring. Therefore, the solid-solution synthesis strategy here is an efficient way to expand and modify the chemical variety of the MIP-208 structural cavity, leading to a series of MTV-MIP-208 materials.

The stability of any MOF is a practical concern in its applications. For instance, photocatalytic methanation requires a combination of thermal, hydrolytic, and UV irradiation stability of the MOF catalyst because the catalysis is normally carried out at temperatures close to 200°C, under UV irradiation and in the presence of stoichiometric water generated as the side product. Therefore, the stability of MIP-208 was tested before applying it to the photocatalytic methanation. The results from both temperature-dependent PXRD measurements and thermogravimetric analysis support the high stability of MIP-208 (Figure S9). Its ordered crystal structure is stable up to 325°C in air, which is comparable to MIP-177-HT, and clearly surpasses MIL-91 and DGIST-1 (unstable above 200°C). Furthermore, the activated MIP-208 sample hardly adsorbs water (less than 5 wt %) when exposed to air for a long time, considerably much less than the Al-CAU-10 series do. This enhanced hydrophobicity of MIP-208 is thus associated with the bridging oxo group effect, in comparison with the OH in CAU-10, as well as the limited hydrophilic character of acetamide.

Soaking MIP-208 in liquid water at room temperature for 3 days and heating it in boiling water for 8 h, separately, tested its hydrolytic stability. The PXRD patterns

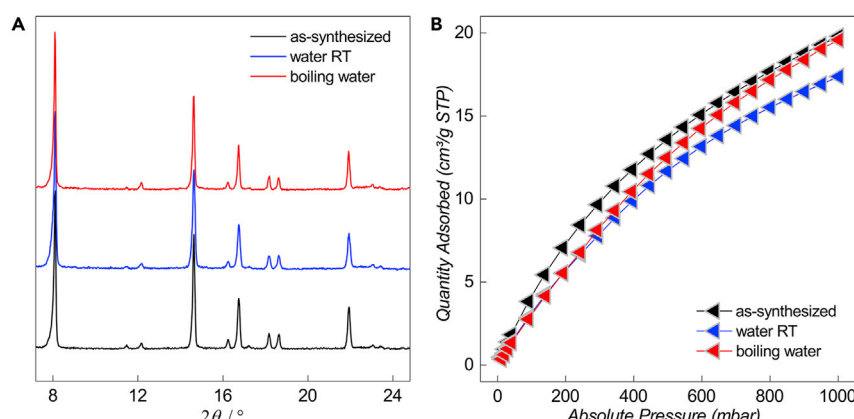


**Figure 4. Results of Water Stability Tests**

(A) PXRD patterns for the MIP-208 samples before and after water treatments.  
(B) CO<sub>2</sub> adsorption isotherms collected at 298 K for the MIP-208 samples before and after water treatments.

of the tested samples were identical to those of the as-synthesized ones (Figure 4A), supporting the robustness of the crystalline long-range order. The CO<sub>2</sub> adsorption data (Figure 4B) confirmed the high hydrolytic stability of MIP-208, with minor differences between the sample before and after water treatments. In addition, the hydrolytic stability of MIP-208 in aqueous solution with various pH values was also investigated, which supports the excellent resistance of MIP-208 toward those chemical treatments (Figure S10). It is worth noting that MIP-208 is among the most hydrothermally stable Ti-MOFs (comparable to that of the Ti-bisphosphonate MIL-91) and outperforms all Ti-carboxylate MOFs reported thus far.

As MIP-208 possesses a 1D TiO chain building block, a good photo-responsive activity is expected. Photocatalytic conversion of CO<sub>2</sub> to methane was thus selected as the model reaction because this reaction could generate a value-added product from CO<sub>2</sub> emissions. Promising progress has been achieved lately in using MOF-based heterogeneous catalysts for CO<sub>2</sub> conversion to methane.<sup>72</sup> For instance, MOF-supported nickel and platinum NPs could promote thermal methanation under harsh conditions, such as high pressures and temperatures. Photocatalytic methanation by MOF-based catalysts has, however, been hampered for a long time by poor selectivity until the recent success reported of a HKUST-1@TiO<sub>2</sub> core-shell composite applied under UV irradiation, albeit its rather low efficiency.<sup>73</sup> Lately, the first example of a pure photoactive MOF displaying catalytic methanation has been reported, which involves ZnO inorganic bricks in a nitrogen-rich framework exhibiting a CH<sub>4</sub> generation productivity of 30 μmol·g<sub>catalyst</sub><sup>-1</sup> after 24 h at 215°C under UV light irradiation. A notable enhancement of activity was attained via supporting Cu<sub>2</sub>O NPs on the Zn-MOF to form a composite catalyst, which led to a CH<sub>4</sub> production of 45 μmol·g<sub>catalyst</sub><sup>-1</sup> under the same conditions.<sup>74</sup> These breakthroughs are undoubtedly encouraging, although the photocatalytic activity of MOF materials remains very low. Therefore, developing efficient and selective MOF-based photocatalysts for methanation is of great interest but still remains a challenge.

Pure MIP-208 samples were first tested for photocatalytic methanation. Preliminary control experiments under similar conditions as those used in the photocatalytic reaction, but in the dark, showed that MIP-208 did not promote thermally CO<sub>2</sub> reduction to CH<sub>4</sub>. In contrast, a CH<sub>4</sub> production of about 40 μmol g<sub>catalyst</sub><sup>-1</sup> could be achieved using MIP-208 as the catalyst in the mixture of CO<sub>2</sub> (0.25 bar) and hydrogen

(1.05 bar) under UV-visible (UV-vis) irradiation (Xenon lamp, 1,350 W × m<sup>-2</sup>) at 200°C after 22 h ([Figure S11](#)). This result highlights the positive influence of the 1D TiO chain SBU in MIP-208 regarding its photo-response because the benchmark compound NH<sub>2</sub>-MIL-125, which is built with discrete Ti<sub>8</sub> clusters, exhibits negligible photocatalytic activity under similar reaction conditions.<sup>74</sup> Furthermore, in comparison with the state-of-the-art MOF photocatalysts for methanation,<sup>74</sup> an enhancement of 33% in efficiency was noticed for MIP-208, suggesting that MIP-208, to our knowledge, could be the most efficient, pure MOF photocatalyst for methanation to date.

In order to further improve the CH<sub>4</sub> formation rate, incorporation of metal NPs onto MIP-208 was considered to form a composite catalyst, as it is well documented that photocatalytic methanation generally requires the presence of a metal or metal oxide with hydrogenation activity, such as nickel, copper, rhodium, palladium, or ruthenium.<sup>75</sup> We initially selected RuO<sub>x</sub> NPs as the composite component, owing to the fact that Ru species generally show the highest activity in the methanation of CO<sub>2</sub> under milder conditions, despite their limited selectivity compared with other active elements.<sup>76,77</sup> In addition, the oxide form, instead of elemental metal NPs, features an elevated stability to facilitate easy handling during the catalysis process. The MIP-208@RuO<sub>x</sub> composite was obtained following the post-synthetic photodeposition of RuO<sub>x</sub> NPs on MIP-208 by the photocatalytic reduction of water-soluble KRuO<sub>4</sub> using methanol as the sacrificial electron donor ([Figure S12](#)). The success of RuO<sub>x</sub> photodeposition by photocatalytic perruthenate reduction further demonstrates the photoactivity of MIP-208, as it has been proven that an evidence supporting the occurrence of photoinduced charge separation upon irradiation of a solid is the observation of photodeposition onto the material of metal NPs from aqueous solutions.<sup>78</sup>

After deposition, the determination of the Ru content and average particle size in the composite was carried out. Energy-dispersive X-ray spectroscopy (EDX) analysis of MIP-208@RuO<sub>x</sub> showed a Ru content of 0.76 wt %. Field emission scanning electron microscopy images of MIP-208@RuO<sub>x</sub> displayed a similar crystallite morphology as that of the pristine MOF, without obvious free RuO<sub>x</sub> particles ([Figure S13](#)). Dark-field scanning transmission electron microscopy (DF-STEM) measurements revealed the presence of small RuO<sub>x</sub> NPs (1.4 ± 0.14 nm). The homogeneous distribution of RuO<sub>x</sub> NPs all over MIP-208 was further confirmed by DF-STEM coupled to an EDX detector ([Figure S14](#)).

Preservation of the crystalline structure of MIP-208 after RuO<sub>x</sub> photodeposition was confirmed by PXRD data ([Figure S15](#)). The lack of additional peaks in the composite pattern compared with that of the pure MIP-208 could be attributed to the low Ru loading and the evenly distributed small particle size, as determined by TEM images.

The MIP-208@RuO<sub>x</sub> solid was also characterized by X-ray photoelectron spectroscopy (XPS, [Figure S16](#)). The C1s spectrum shows the presence of aromatic carbons (284.4 eV). In addition, a band centered at 285.9 eV attributable to the C–N bond of the amide groups was observed, together with another band centered at 289 eV that can be assigned to the carbonyl of both the amide and the carboxylate groups. The amide group is clearly observed in the N1s band centered at about 399 eV as well. The broad O1s band is mainly due to the presence of oxygen atoms in the carboxylate and amide groups, together with the Ti–O, and Ru–O bonds. Ti 2p spectrum can be assigned to the presence of Ti<sup>4+</sup> ions. Ruthenium is recognized by the bands appearing at about 280.7 and 282.4 eV that can be assigned to the Ru 3d<sub>5/2</sub> of RuO<sub>2</sub>.

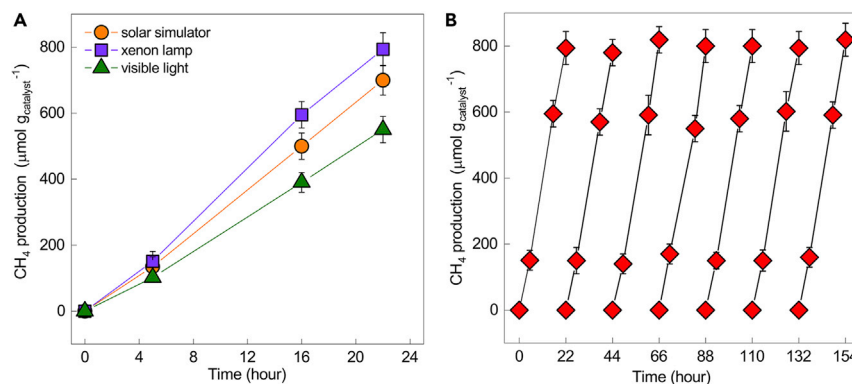


**Figure 5. Photocatalytic Performance of MIP-208@RuO<sub>x</sub> in CO<sub>2</sub> Methanation**

(A) Temporal evolution of CH<sub>4</sub> during the photocatalytic CO<sub>2</sub> reduction with MIP-208@RuO<sub>x</sub> as the catalyst using a solar simulator and a xenon lamp with full-range lights and visible light (Xe lamp with >455 nm filter).

(B) Reusability of MIP-208@RuO<sub>x</sub> in the photocatalytic methanation of CO<sub>2</sub> (seven-times cycling) using a xenon lamp as the irradiation source. Reaction conditions: catalyst (15 mg), H<sub>2</sub> (1.05 bar), CO<sub>2</sub> (0.25 bar), temperature (200°C), irradiation source a xenon lamp (1,350 W × m<sup>-2</sup>) or solar simulator (1,000 W × m<sup>-2</sup>).

and hydrated RuO<sub>2</sub>, respectively.<sup>79,80</sup> The expected Ru 3d<sub>3/2</sub> band appearing at higher binding energies (~4.1 eV) (Figure S16) is, however, difficult to observe because it overlaps with the C–N contribution of the acetamido groups.<sup>78,80</sup> XPS analysis also can provide an estimation of the valence band maximum of the MIP-208@RuO<sub>x</sub> solid by measuring the lowest energy electron band of the material referred to the work function of the instrument. As shown in Figure S17, a valence band potential of −1.51 V was estimated. This value together with the 2.92 eV band gap measured from the Tauc plot of the diffuse reflectance UV-vis spectrum gives a value for the LUCO of −2.874 V.

The photocatalytic performance of the MIP-208@RuO<sub>x</sub> composite in the methanation of CO<sub>2</sub> was then evaluated under the same reaction conditions as those used for testing the pristine MOF. Control experiments using MIP-208@RuO<sub>x</sub> in the dark under the same reaction conditions showed negligible CH<sub>4</sub> production. As expected, a selective CO<sub>2</sub> conversion into CH<sub>4</sub> (800  $\mu\text{mol g}_{\text{catalyst}}^{-1}$ ) as the only product was observed (Figure 5A). Specifically, the amounts of CO and C<sub>2</sub>H<sub>6</sub> were under the detection limit of our micro gas chromatograph (micro-GC). This CH<sub>4</sub> production value is 20 times higher compared with that obtained using the pure MIP-208 sample. Regarding product selectivity, photocatalytic CO<sub>2</sub> hydrogenation renders generally methane or CO as the main products, accompanied by minor amounts of C<sub>2</sub> and C<sub>3</sub>.<sup>81</sup> Selectivity to methane or CO depends mainly on the strength of CO adsorption and the hydrogenating activity of the photocatalysts. In general, if CO remains strongly adsorbed on the photocatalyst, further hydrogenation takes place and the final product is methane. It is proposed that MIP-208 favors CO adsorption near the RuO<sub>x</sub>-active sites and thus leads to high methane selectivity.

Similar time-conversion plots, with a slightly lower CH<sub>4</sub> formation rate, were also measured using simulated sunlight irradiation (1 Sun) (Figure 5A). The difference between the CH<sub>4</sub> production using a xenon lamp or simulated sunlight can be attributed to the lower power of the simulated sunlight (1,000 W × m<sup>-2</sup>) compared with the xenon lamp (1,350 W × m<sup>-2</sup>). Furthermore, photomethanation of CO<sub>2</sub> using MIP-208@RuO<sub>x</sub> as catalyst was also performed upon visible-light irradiation by

filtering the output beam of the Xe lamp ( $\lambda > 455$  nm). A similar temporal CH<sub>4</sub> formation profile was recorded, with a CH<sub>4</sub> production at final time for visible light about 78% with respect to the use of the full UV-vis light emission provided by the Xe lamp (Figure 5A). This similarity in the temporal CO<sub>2</sub> conversion indicates that a major percentage of the MIP-208@RuO<sub>x</sub> photoresponse must derive from the visible region. Both experiments under simulated sunlight illumination and visible-light irradiation indicate that a considerable proportion of the MIP-208-RuO<sub>x</sub> photoresponse derives from the visible region. This photoresponse indicates that RuO<sub>x</sub> is acting as a light harvester in addition to being an active site, since MIP-208 in the absence of RuO<sub>x</sub> exhibits much less photomethanation rate and should not be responsive under visible light.

The recycling stability of the MIP-208@RuO<sub>x</sub> composite as a photocatalyst was determined by performing a series of consecutive recycling runs following the temporal evolution of CO<sub>2</sub> conversion and CH<sub>4</sub> formation. These stability tests are important considering the conditions of photocatalytic methanation, particularly the presence of H<sub>2</sub>O and the reaction temperature of 200°C. The results presented in Figure 5B show coincident plots for the temporal CH<sub>4</sub> evolution upon seven consecutive runs, supporting the stability of the material under the conditions of the photocatalytic reaction. It is noteworthy that this highly selective and constant methanation activity promoted by RuO<sub>x</sub> has hardly been achieved before, as CO has been proven to be the side product in this reaction, which led to a considerable deactivation of the catalyst.<sup>77</sup> In addition, irradiation of the MIP-208@RuO<sub>x</sub> composite in an argon atmosphere using the xenon lamp or solar simulator at 200°C revealed the evolution of a tiny amount of CO<sub>2</sub>, corresponding to the decomposition of a small fraction of the IPA linkers present in the material (<0.05 μmol CO<sub>2</sub>/μmol ligand). This small CO<sub>2</sub> evolution from MIP-208@RuO<sub>x</sub> compares favorably with the stability of the most robust MOFs reported as photocatalysts under similar irradiation conditions.<sup>82</sup>

The crystallinity of the MIP-208@RuO<sub>x</sub> sample after seven catalytic cycles was well maintained, as no notable change in the PXRD pattern was observed (Figure S18). Furthermore, the solid-state <sup>13</sup>C-NMR spectra of the fresh and seven-times reused MIP-208@RuO<sub>x</sub> were coincident (Figure S19). DF-STEM images of the catalyst after recycling were also similar to those of the fresh sample, without any evidence of RuO<sub>x</sub> particle growth or agglomeration (Figure S20). Thus, both photocatalytic activity and characterization of the seven-times used MIP-208@RuO<sub>x</sub> sample indicate the stability of the material under irradiation conditions.

To determine the origin of CH<sub>4</sub>, an experiment using <sup>13</sup>C-labeled CO<sub>2</sub> was carried out, monitoring the isotopic composition of CH<sub>4</sub> evolved by mass spectrometry. The results presented in Figure S21 show the peaks corresponding to <sup>13</sup>CH<sub>4</sub> appearing at 17 Dalton. It is important to note that the injection of a sample before irradiation does not show in the chromatogram any peak at the retention time of <sup>13</sup>CH<sub>4</sub>.

To shed light on the main operating mechanism of the photocatalytic methanation, H<sub>2</sub> was replaced by dimethylaniline as the sacrificial electron donor. Two possible operating mechanisms have been reported for the photocatalytic methanation of CO<sub>2</sub>, either the so-called photothermal pathway or the photoinduced charge separation pathway.<sup>78</sup> In the photothermal mechanism, light energy is converted into local heat on the metal NPs and the temperature increases on the NP surface promote the thermal conversion of CO<sub>2</sub> and H<sub>2</sub> into the product.<sup>78</sup> This local temperature increase is undetectable by measurements of the macroscopic system due to

the low proportion of RuO<sub>x</sub>. In the photocatalytic mechanism, light absorption leads to a charge separation with the generation of electrons in the conduction band and holes in the valence band, which causes CO<sub>2</sub> reduction and H<sub>2</sub> oxidation, respectively. In the photoinduced charge separation state, the use of an electron donor better than H<sub>2</sub> should equally result in CO<sub>2</sub> conversion to methane, with an even higher reaction rate than using H<sub>2</sub> as a reagent. On the contrary, this electron donor should not be adequate for the photothermal reaction. In the present study, dimethylaniline (0.76 V versus Ag-AgCl) was selected as an electron donor.<sup>83</sup> The results show that CH<sub>4</sub> is formed in the presence of dimethylaniline (40 μL) even at a higher rate than in the presence of H<sub>2</sub> as a reagent, reaching a CH<sub>4</sub> production rate in 5 h of 250 μmol g<sub>catalyst</sub><sup>-1</sup> compared with 180 μmol g<sub>catalyst</sub><sup>-1</sup> when using H<sub>2</sub> as a reagent. Interestingly, a similar experiment using anisole as an electron donor with higher oxidation potential (1.93 V versus Ag-AgCl) than dimethylaniline (0.90 V versus Ag-AgCl) resulted in a lower CH<sub>4</sub> production (25 μmol g<sub>catalyst</sub><sup>-1</sup>). This observation is in agreement with a previous report using Cu<sub>2</sub>O supported on graphene as photocatalyst and observing that the methane production rates decrease as the oxidation potential of the sacrificial electron donor increases.<sup>84,85</sup> Furthermore, if photomethanation is attempted under the same conditions, but in the presence of nitrobenzene (40 μL, -0.36 V versus Ag-AgCl)<sup>86</sup> as electron quencher competing with CO<sub>2</sub>, then no formation of CH<sub>4</sub> is observed. This dependence of CH<sub>4</sub> formation on the presence and redox potential of electron donor and acceptor quenchers is fully consistent with the prevalent operation of a photocatalytic mechanism involving photoinduced e<sup>-</sup>/h<sup>+</sup> separation and CH<sub>4</sub> formation by consecutive eight e<sup>-</sup> (plus 8 H<sup>+</sup>) reduction of CO<sub>2</sub>.

The occurrence of the photoinduced charge separation and the reaction of this photo-induced charge-separated state with electron donors was additionally confirmed by photocurrent measurements. A thin film of MIP-208@RuO<sub>x</sub> was further deposited on a transparent fluorine-doped tin oxide electrode. Starting from a polarization potential of 1.6 V, the MIP-208@RuO<sub>x</sub> electrode was submitted to a decreasing bias potential in a single electrochemical cell using tetrapropylammonium tetrafluoroborate in acetonitrile as an electrolyte. The current density clearly increased at each voltage upon illumination of the photoanode with the output of a Xe lamp (Figure S22). Furthermore, the presence of methanol as an electron donor increased the photocurrent significantly, indicating that this reagent was acting as a sacrificial electron donor, becoming oxidized and donating electrons to the MIP-208@RuO<sub>x</sub> in its excited state.

Besides the photocatalytic mechanism of CO<sub>2</sub> reduction to CH<sub>4</sub>, there are reports in the literature showing that CO<sub>2</sub> reduction can take place alternatively through a photothermal pathway.<sup>75,87</sup> In this mechanism, photon energy is dissipated in the active site that undergoes a local heating at the nanometer scale sufficient to overcome the activation barrier for a thermocatalytic pathway. The local temperature of these nanometric hot spots cannot be determined macroscopically, particularly considering the low proportion of these hot spots in the composition of the photocatalyst and the thermal conductivity of the medium. One common methodology to assess the occurrence of local heating is the use of quantum dots (QDs) for monitoring the emission intensity decrease as local thermometer.<sup>84</sup> This method is based on the decrease of the emission intensity of QDs as the temperature experienced by NP increases in a certain temperature range. In a preliminary calibration study, it was determined that the photoluminescence lifetime emission of CdSe-ZnS QDs decreases as the temperature increases (Figure S23). This observation is a consequence of the emission intensity decrease of core-shell CdSe-ZnS NPs as the temperature increases in the range from 25°C to 200°C (Figure S24). Thus, core-shell CdSe-ZnS NPs can be used as a local nanometric thermometer to get

some information about local temperature changes during irradiation that could distinguish between photocatalytic or photothermal reaction mechanism when using MIP-208@RuO<sub>x</sub> in photomethanation. After calibration, the CdSe-ZnS NPs were dispersed on the MIP-208@RuO<sub>x</sub> sample. Comparison of the emission intensity of CdSe-ZnS adsorbed on MIP-208@RuO<sub>x</sub> depending on whether the solid is in the dark or illuminated with the Xe lamp conclusively shows that even if the macroscopic temperature is supposed to be constant, CdSe-ZnS QDs experience a local heating under Xe irradiation, required for a photothermal mechanism (Figure S25). However, it must be noted that although the experiments with CdSe-ZnS as local temperature probes conclusively show the temperature increase at the nanometric scale and not observed macroscopically, the quenching experiments mentioned previously and particularly the fact that a good electron acceptor completely stops methane formation indicate that the mechanism is fully photocatalytic derived from charge separation but accompanied with temperature increase at the NPs that does not lead to product formation. Otherwise, nitrobenzene, quenching electrons but not impeding heating, would have not completely stopped the CH<sub>4</sub> formation.

The influence of the temperature was addressed by performing photomethanation by MIP-208@RuO<sub>x</sub> at different temperatures in the range from 100°C to 200°C (Figure S26). It was observed that CH<sub>4</sub> formation starts at 100°C but undergoes a significant increase in formation rate at temperatures higher than 150°C. Control experiments in the dark indicate that CH<sub>4</sub> formation is one order of magnitude less or lower than upon irradiation. This behavior indicates that the photocatalytic process has an activation energy.

To understand the origin of the thermal activation of the photocatalytic reaction, the possible role of H<sub>2</sub>O as a poison was considered. H<sub>2</sub>O is a reaction product that can be strongly adsorbed on the active sites competing favorably with CO<sub>2</sub> adsorption and stopping the reaction. In this case, one of the roles of heating would be H<sub>2</sub>O desorption from the active sites. Aimed at providing some support to this proposal, a control experiment was performed adding H<sub>2</sub>O (60 µL) at the initial reaction stage of the photocatalytic methanation. A significant decrease in the initial methanation rate by one order of magnitude from 40 to about 4 µmol g<sub>catalyst</sub><sup>-1</sup> h<sup>-1</sup> was measured (Figure S26). This negative role of H<sub>2</sub>O should also take place in the reactor as photomethanation starts and temperatures above 100°C would allow its desorption.

In summary, benefiting from a synergetic adjustment including both the preformed Ti<sub>8</sub>AF cluster rearrangement and the *in situ* linker formation, which slows down the reaction, MIP-208, the first Ti-IPA MOF, was synthesized with high crystallinity and tunable scale. Its crystal structure, which is isostructural to CAU-10, constitutes *cis*-connected corner-sharing TiO<sub>6</sub> polyhedra that extend along the c axis, resulting in a 1D helical chain inorganic building unit. Multivariate MIP-208 structures with tunable chemical environments and sizable porosities could be achieved by adopting the solid-solution mixed-linker synthesis strategy. This material has been proven to be the best photocatalyst for the methanation of CO<sub>2</sub> in terms of activity and selectivity among all the pure MOFs, owing to its excellent stability and photoresponse. Further improvement of catalytic activity was achieved by the photodeposition of RuO<sub>x</sub>. The resulting MIP-208@RuO<sub>x</sub> composite exhibits, under identical conditions, an enhancement of efficiency of a factor of about 20 in comparison with that of the pure MOF. The composite catalyst displays high stability and reusability. These results illustrate the continuous interest in the synthesis of novel Ti-MOFs that could lead to improved generations of photocatalysts, suitable for the production of solar fuels and the photoinduced methanation of CO<sub>2</sub>.

## EXPERIMENTAL PROCEDURES

### Resource Availability

#### Lead Contact

Further information and requests for resources could be directed to and will be fulfilled by the Lead Contact, Sujing Wang ([sjwang4@ustc.edu.cn](mailto:sjwang4@ustc.edu.cn)).

#### Materials Availability

All chemicals were purchased from commercial suppliers and used as received without further purification. 5-NH<sub>2</sub>-IPA (Alfa Aesar), IPA (Alfa Aesar), 5-Me-IPA (TCI), 5-Br-IPA (Sigma), 5-F-IPA (FluoroChem), 5-tBu-IPA (FluoroChem), PDA (FluoroChem), formic acid (Fisher), acetic acid (Acros), acetic anhydride (Sigma), MeOH (Fisher), and Ti(iPrO)<sub>4</sub> (Alfa Aesar).

#### Data and Code Availability

Data supporting the findings of this paper are available from the corresponding authors upon reasonable request.

### Method Details

#### Synthesis of MIP-208 (Small Scale)

To a 23-mL Teflon reactor, Ti<sub>8</sub>AF cluster solid (220 mg) was added followed by the addition of acetic anhydride (5 mL) and acetic acid (5 mL). The mixture was stirred at room temperature for 20 min before 5-NH<sub>2</sub>-IPA (362 mg, 2 mmol) was added once. After stirring for 10 min, MeOH (0.5 mL) was added, and the overall mixture was stirred at room temperature for another 10 min. Afterward, the reaction was heated in an oven at 180°C for 48 h. When the reaction was cooled to room temperature, the dark yellow-light brown product was collected by filtration, washed with acetone and then air dried. Yield: 330 mg (average of five parallel reactions).

#### Synthesis of MIP-208 (Scale-Up)

To a 125-mL Teflon reactor, Ti<sub>8</sub>AF cluster solid (3.5 g) was added followed by the addition of acetic anhydride (25 mL) and acetic acid (25 mL). The mixture was stirred at room temperature for 20 min before 5-NH<sub>2</sub>-IPA (3.62 g, 20 mmol) was added once. After stirring for 10 min, MeOH (3.5 mL) was added, and the overall mixture was stirred at room temperature for another 10 min. Afterward, the reaction was heated in an oven at 180°C for 48 h. When the reaction was cooled to room temperature, the dark yellow-light brown product was collected by filtration, washed with acetone and then air dried. Yield: 4.3 g (average of five parallel reactions).

#### Typical Synthesis of MTV-MIP-208

To a 23-mL Teflon reactor, Ti<sub>8</sub>AF cluster solid (220 mg) was added followed by the addition of acetic anhydride (5 mL) and acetic acid (5 mL). The mixture was stirred at room temperature for 20 min before a linker mixture of 5-NH<sub>2</sub>-IPA (1 mmol) and the secondary IPA ligand (1 mmol) was added. After stirring for 10 min, MeOH (0.5 mL) was added, and the overall mixture was stirred at room temperature for another 10 min. Afterward, the reaction was heated in an oven at 180°C for 48 h. When the reaction was cooled to room temperature, the dark yellow-light brown product was collected by filtration, washed with acetone, and then air dried.

### Photocatalytic Methanation Tests

The photocatalytic methanation of CO<sub>2</sub> experiments was carried out using a quartz photoreactor (51 mL) equipped with a heating mantle to control the desired temperature. In a typical experiment, the powdered photocatalyst (15 mg) was placed as a bed in the reactor, and then the system was purged first with H<sub>2</sub> and later with CO<sub>2</sub>.

until a ratio of 4 to 1 was obtained. Subsequently, the photoreactor was heated at 200°C, and then the photocatalyst was irradiated using a Xe lamp (150 W) or a solar simulator. At the desired reaction time, an aliquot was sampled from the photoreactor and analyzed in an Agilent 490 MicroGC equipped with two channels and thermal conductivity detectors. One channel equipped with a MolSieve 5 Å column allowed the analysis of H<sub>2</sub>, O<sub>2</sub>, N<sub>2</sub>, and CO, whereas the other channel equipped with a Pore Plot Q column allowed the determination of CO<sub>2</sub>, CH<sub>4</sub>, and short-chain hydrocarbons. Quantification was performed using calibration plots employing commercially available gas mixtures.

### X-Ray Crystallographic Data

The single-crystal X-ray crystallographic data for MIP-208 were collected on the PROXIMA 2A beamline at Synchrotron SOLEIL and have been deposited at the Cambridge Crystallographic Data Centre (CCDC), under deposition number CCDC: 1989406. High-resolution PXRD data of MIP-208 for Rietveld refinement were collected on the STOE STADI PESSENTIAL X-ray diffractometer equipped with a Mythen II detector in the Debye–Scherrer mode with pure Cu K $\alpha$ 1 radiation ( $\lambda = 1.5406 \text{ \AA}$ ) (capillary: 0.2 mm, angle range: 5°–120°, step size: 0.015°, total counting time: 16.5 h, room temperature) and have been deposited at CCDC under the deposition number CCDC: 2011709. These data can be obtained free of charge from the CCDC database via [www.ccdc.cam.ac.uk](http://www.ccdc.cam.ac.uk). All other relevant data supporting the findings of this study are available from the corresponding authors on request.

### SUPPLEMENTAL INFORMATION

Supplemental Information can be found online at <https://doi.org/10.1016/j.chempr.2020.10.017>.

### ACKNOWLEDGMENTS

S.W. acknowledges the support from the National Natural Science Foundation of China (22071234) and the Fundamental Research Funds for the Central Universities (WK2480000007). S.N. thanks the Ministerio de Ciencia, Innovación y Universidades (RTI2018-099482-A-I00 project, the Fundación Ramón Areces (XVIII Concurso Nacional para la Adjudicación de Ayudas a la Investigación en Ciencias de la Vida y de la Materia, 2016), and Generalitat Valenciana grupos de investigación consolidables (AICO/2019/214 project) and Agencia Valenciana de la Innovación (INNEST/2020/111 project) for financial support. C.-C.C. acknowledges the support from the Program of China Scholarship Council (201700260093) and PHC Cai YuanPei Project (38893VJ). C.M.-C. is grateful for financial support from the Institut Universitaire de France (IUF) and the Paris Ile-de- France Region – DIM “Respose.” H.G. thanks the Spanish Ministry of Science and Innovation (Severo Ochoa and RTI2018-098237-CO2-1) and Generalitat Valenciana (Prometeo2017/083) for financial support. The authors thank the staff at Synchrotron SOLEIL and the associated scientists for beamtime and assistance during SCXRD data collections on PROXIMA 2A, as well as Dr. Peng Guo and Dr. Nana Yan from Dalian Institute of Chemical Physics (Chinese Academy of Sciences) for the collection of high-resolution PXRD data for Rietveld refinement.

### AUTHOR CONTRIBUTIONS

Conceptualization, S.W., C.S., S.N., and H.G.; Investigation, S.W., M.C.-A., S.N., C.-C.C., A.T., J.M., C.M.-C., L.Y., H.W., W.S., H.G., and C.S.; Writing – Original Draft,

S.W.; Writing – Review & Editing, S.W., S.N., A.T., C.M.-C., W.S., H.G., and C.S; Supervision, H.G. and C.S.

## DECLARATION OF INTERESTS

The authors declare no competing interests.

Received: March 24, 2020

Revised: April 23, 2020

Accepted: October 19, 2020

Published: November 12, 2020

## REFERENCES

1. Dhakshinamoorthy, A., Li, Z., and Garcia, H. (2018). Catalysis and photocatalysis by metal organic frameworks. *Chem. Soc. Rev.* 47, 8134–8172.
2. Chen, L., and Xu, Q. (2019). Metal-organic framework composites for catalysis. *Matter* 1, 57–89.
3. García, H., and Navalón, S. (2018). *Metal-Organic Frameworks: Applications in Separations and Catalysis* (Wiley-VCH Verlag GmbH & Co. KGaA).
4. Yeung, H.H., Li, W., Saines, P.J., Köster, T.K., Grey, C.P., and Cheetham, A.K. (2013). Ligand-directed control over crystal structures of inorganic-organic frameworks and formation of solid solutions. *Angew. Chem. Int. Ed. Engl.* 52, 5544–5547.
5. Lu, W., Wei, Z., Gu, Z.Y., Liu, T.F., Park, J., Park, J., Tian, J., Zhang, M., Zhang, Q., Gentle, T., III, et al. (2014). Tuning the structure and function of metal-organic frameworks via linker design. *Chem. Soc. Rev.* 43, 5561–5593.
6. Desai, A.V., Sharma, S., Let, S., and Ghosh, S.K. (2019). N-donor linker based metal-organic frameworks (MOFs): advancement and prospects as functional materials. *Coord. Chem. Rev.* 395, 146–192.
7. Zhang, H., Zou, R., and Zhao, Y. (2015). Macrocyclic-based metal-organic frameworks. *Coord. Chem. Rev.* 292, 74–90.
8. He, Y., Li, B., O'Keeffe, M., and Chen, B. (2014). Multifunctional metal-organic frameworks constructed from meta-benzenedicarboxylate units. *Chem. Soc. Rev.* 43, 5618–5656.
9. Wang, H., Zhu, Q.-L., Zou, R., and Xu, Q. (2017). Metal-organic frameworks for energy applications. *Chem* 2, 52–80.
10. Kuppler, R.J., Timmons, D.J., Fang, Q.-R., Li, J.-R., Makal, T.A., Young, M.D., Yuan, D., Zhao, D., Zhuang, W., and Zhou, H. (2009). Potential applications of metal-organic frameworks. *Coord. Chem. Rev.* 253, 3042–3066.
11. Czaja, A.U., Trukhan, N., and Müller, U. (2009). Industrial applications of metal-organic frameworks. *Chem. Soc. Rev.* 38, 1284–1293.
12. Silva, P., Vilela, S.M., Tomé, J.P., and Almeida Paz, F.A. (2015). Multifunctional metal-organic frameworks: from academia to industrial applications. *Chem. Soc. Rev.* 44, 6774–6803.
13. Ren, J., Dyoisiba, X., Musyoka, N.M., Langmi, H.W., Mathe, M., and Liao, S. (2017). Review on the current practices and efforts towards pilot-scale production of metal-organic frameworks (MOFs). *Coord. Chem. Rev.* 352, 187–219.
14. Lorz, P.M., Towae, F.K., Enke, W., Jäckh, R., Bhargava, N., and Hillesheim, W. (2007). Phthalic acid and derivatives. In Ullmann's Encyclopedia of Industrial Chemistry (Wiley-VCH Verlag GmbH). [https://doi.org/10.1002/14356007.a20\\_181.pub2](https://doi.org/10.1002/14356007.a20_181.pub2).
15. Sheehan, R.J. (2011). Terephthalic acid, dimethyl terephthalate, and isophthalic acid. In Ullmann's Encyclopedia of Industrial Chemistry (Wiley-VCH Verlag GmbH). [https://doi.org/10.1002/14356007.a26\\_193.pub2](https://doi.org/10.1002/14356007.a26_193.pub2).
16. Ohtani, M., Takase, K., Wang, P., Higashi, K., Ueno, K., Yasuda, N., Sugimoto, K., Furuta, M., and Kobiro, K. (2016). Water-triggered macroscopic structural transformation of a metal-organic framework. *CrystEngComm* 18, 1866–1870.
17. Reinsch, H., De Vos, D., and Stock, N. (2013). Structure and properties of  $[Al_4(OH)_8(o-C_6H_4(CO_2)_2)_2] \cdot H_2O$ , a layered aluminum phthalate. *Z. Anorg. Allg. Chem.* 639, 2785–2789.
18. Li, H., Davis, C.E., Groy, T.L., Kelley, D.G., and Yaghi, O.M. (1998). Coordinatively unsaturated metal centers in the extended porous framework of  $Zn_3(BDC)_3 \cdot 6CH_3OH$  ( $BDC = 1,4\text{-benzenedicarboxylate}$ ). *J. Am. Chem. Soc.* 120, 2186–2187.
19. Banerjee, D., and Parise, J.B. (2011). Recent advances in s-block metal carboxylate networks. *Cryst. Growth Des.* 11, 4704–4720.
20. Pagis, C., Ferbinteanu, M., Rothenberg, G., and Tanase, S. (2016). Lanthanide-based metal organic frameworks: synthetic strategies and catalytic applications. *ACS Catal.* 6, 6063–6072.
21. Aguirre-Díaz, L.M., Reinares-Fisac, D., Iglesias, M., Gutiérrez-Puebla, E., Gándara, F., Snejko, N., and Monge, M.Á. (2017). Group 13th metal-organic frameworks and their role in heterogeneous catalysis. *Coord. Chem. Rev.* 335, 1–27.
22. Kang, M.P., Luo, D.B., Deng, Y.R., Li, R.X., and Lin, Z.E. (2014). Solvothermal synthesis and characterization of new calcium carboxylates based on cluster- and rod-like building blocks. *Inorg. Chem. Commun.* 47, 52–55.
23. Bourne, S.A., Lu, J.J., Mondal, A., Moulton, B., and Zaworotko, M.J. (2001). Self-assembly of nanometer-scale secondary building units into an undulating two-dimensional network with two types of hydrophobic cavity. *Angew. Chem. Int. Ed. Engl.* 40, 2111–2113.
24. Vodak, D.T., Braun, M.E., Kim, J., Eddaoudi, M., and Yaghi, O.M. (2001). Metal-organic frameworks constructed from pentagonal antiprismatic and cuboctahedral secondary building units. *Chem. Commun. (Camb)*. 2001, 2534–2535.
25. Barthelet, K., Riou, D., and Ferey, G. (2002).  $[V^{IV}(H_2O)]_3O(O_2CC_6H_4CO_2)_3 \cdot (Cl, 9H_2O)$  (MIL-59): a rare example of vanadocarboxylate with a magnetically frustrated three-dimensional hybrid framework. *Chem. Commun.* 2002, 1492–1493.
26. Qazvini, O.T., Babarao, R., Shi, Z.L., Zhang, Y.B., and Teifer, S.G. (2019). A robust ethane-trapping metal-organic framework with a high capacity for ethylene purification. *J. Am. Chem. Soc.* 141, 5014–5020.
27. Kim, J.-Y., Norquist, A.J., and O'Hare, D. (2003). Incorporation of uranium(vi) into metal-organic framework solids,  $[UO_2(C_4H_4O_4)] \cdot H_2O$ ,  $[UO_2F(C_4H_4O_4)] \cdot 2H_2O$ , and  $[(UO_2)_{1.5}(C_8H_4O_4)_{2.2}](CH_3)_2NCOH_2] \cdot H_2O$ . *Dalton Trans.* 14, 2813–2814.
28. Wang, G., Song, T., Fan, Y., Xu, J., Wang, M., Zhang, H., Wang, L., Huang, L., and Wang, L. (2010).  $[Y_2(H_2O)(BDC)_3(DMF)] \cdot (DMF)_3$ : a rare 2-D  $(4^2 \cdot 6)(4^5 \cdot 6)(4^8 \cdot 6^2)(4^9 \cdot 6^3 \cdot 8)$  net with multi-helical-array and opened windows. *Inorg. Chem. Commun.* 13, 502–505.
29. Mihalcea, I., Henry, N., Clavier, N., Dacheux, N., and Loiseau, T. (2011). Occurrence of an octanuclear motif of uranyl isophthalate with cation-cation interactions through edge-sharing connection mode. *Inorg. Chem.* 50, 6243–6249.
30. Vougo-Zanda, M., Wang, X., and Jacobson, A.J. (2007). Influence of ligand geometry on the formation of In-O chains in metal-oxide organic frameworks (MOOFs). *Inorg. Chem.* 46, 8819–8824.
31. Bu, F., and Xiao, S.J. (2010). A 4-connected anionic metal-organic nanotube constructed from indium isophthalate. *CrystEngComm* 12, 3385–3387.
32. Panda, T., Kundu, T., and Banerjee, R. (2013). Structural isomerism leading to variable proton conductivity in indium(III) isophthalic acid

- based frameworks. *Chem. Commun.* 49, 6197–6199.
33. Chen, P.K., Che, Y.X., Zheng, J.M., and Batten, S.R. (2007). Heteropolynuclear metamagnet showing spin canting and single-crystal to single-crystal phase transformation. *Chem. Mater.* 19, 2162–2167.
34. Zhang, L., Qin, Y.Y., Li, Z.J., Lin, Q.P., Cheng, J.K., Zhang, J., and Yao, Y.G. (2008). Topology analysis and non-linear-optical-active properties of luminescent metal-organic framework materials based on zinc/lead isophthalates. *Inorg. Chem.* 47, 8286–8293.
35. Zhang, J.P., Ghosh, S.K., Lin, J.B., and Kitagawa, S. (2009). New heterometallic carboxylate frameworks: synthesis, structure, robustness, flexibility, and porosity. *Inorg. Chem.* 48, 7970–7976.
36. McCormick, L.J., Morris, S.A., Slawin, A.M.Z., Teat, S.J., and Morris, R.E. (2016). Coordination polymers of 5-alkoxy isophthalic acids. *Cryst. Growth Des.* 16, 5771–5780.
37. Chen, J., Li, C.-P., and Du, M. (2011). Substituent effect of R-isophthalates (R = –H, –CH<sub>3</sub>, –OCH<sub>3</sub>, –tBu, –OH, and –NO<sub>2</sub>) on the construction of CdII coordination polymers incorporating a dipyridyl tecton 2,5-bis(3-pyridyl)-1,3,4-oxadiazole. *CrystEngComm* 13, 1885–1893.
38. Du, M., Zhang, Z.-H., You, Y.-P., and Zhao, X.-J. (2008). R-isophthalate (R = –H, –NO<sub>2</sub>, and –COOH) as modular building blocks for mixed-ligand coordination polymers incorporated with a versatile connector 4-amino-3,5-bis(3-pyridyl)-1,2,4-triazole. *CrystEngComm* 10, 306–321.
39. Chen, L., Ye, J.W., Wang, H.P., Pan, M., Yin, S.Y., Wei, Z.W., Zhang, L.Y., Wu, K., Fan, Y.N., and Su, C.Y. (2017). Ultrafast water sensing and thermal imaging by a metal-organic framework with switchable luminescence. *Nat. Commun.* 8, 15985.
40. Yuan, S., Qin, J.S., Lollar, C.T., and Zhou, H.C. (2018). Stable metal-organic frameworks with group 4 metals: current status and trends. *ACS Cent. Sci.* 4, 440–450.
41. Rieth, A.J., Wright, A.M., and Dincă, M. (2019). Kinetic stability of metal-organic frameworks for corrosive and coordinating gas capture. *Nat. Rev. Mater.* 4, 708–725.
42. Dhakshinamoorthy, A., Asiri, A.M., and García, H. (2016). Metal-organic framework (MOF) compounds: photocatalysts for redox reactions and solar fuel production. *Angew. Chem. Int. Ed. Engl.* 55, 5414–5445.
43. Alvaro, M., Carbonell, E., Ferrer, B., Llabrés i Xamena, F.X., and Garcia, H. (2007). Semiconductor behavior of a metal-organic framework (MOF). *Chemistry* 13, 5106–5112.
44. Nasalevich, M.A., Goesten, M.G., Savenije, T.J., Kapteijn, F., and Gascon, J. (2013). Enhancing optical absorption of metal-organic frameworks for improved visible light photocatalysis. *Chem. Commun.* 49, 10575–10577.
45. Zhu, J.J., Li, P.Z., Guo, W.H., Zhao, Y.L., and Zou, R.Q. (2018). Titanium-based metal-organic frameworks for photocatalytic applications. *Coord. Chem. Rev.* 359, 80–101.
46. Benoit, V., Pillai, R.S., Orsi, A., Normand, P., Jobic, H., Nouar, F., Billemont, P., Bloch, E., Bourrelly, S., Devic, T., et al. (2016). MIL-91(Ti), a small pore metal-organic framework which fulfills several criteria: an upscaled green synthesis, excellent water stability, high CO<sub>2</sub> selectivity and fast CO<sub>2</sub> transport. *J. Mater. Chem. A* 4, 1383–1389.
47. Sun, Y., Liu, Y., Caro, J., Guo, X., Song, C., and Liu, Y. (2018). In-plane epitaxial growth of highly c-oriented NH<sub>2</sub>-MIL-125(Ti) membranes with superior H<sub>2</sub>/CO<sub>2</sub> selectivity. *Angew. Chem. Int. Ed. Engl.* 57, 16088–16093.
48. Wahiduzzaman, M., Wang, S.J., Schnee, J., Vimont, A., Ortiz, V., Yot, P.G., Retoux, R., Daturi, M., Lee, J.S., and Chang, J.-S. (2019). A high proton conductive hydrogen-sulfate decorated titanium carboxylate metal-organic framework. *ACS Sustainable Chem. Eng.* 7, 5776–5783.
49. Pinto, R.V., Wang, S., Tavares, S.R., Pires, J., Antunes, F., Vimont, A., Clet, G., Daturi, M., Maurin, G., Serre, C., and Pinto, M.L. (2020). Tuning cellular biological functions through the controlled release of NO from a porous Ti-MOF. *Angew. Chem. Int. Ed. Engl.* 59, 5135–5143.
50. Assi, H., Mouchaham, G., Steunou, N., Devic, T., and Serre, C. (2017). Titanium coordination compounds: from discrete metal complexes to metal-organic frameworks. *Chem. Soc. Rev.* 46, 3431–3452.
51. Tachikawa, T., Tojo, S., Fujitsuka, M., Sekino, T., and Majima, T. (2006). Photoinduced charge separation in titania nanotubes. *J. Phys. Chem. B* 110, 14055–14059.
52. Wang, S., Kitao, T., Guillou, N., Wahiduzzaman, M., Martineau-Corcos, C., Nouar, F., Tissot, A., Binet, L., Ramsahye, N., Devautour-Vinot, S., et al. (2018). A phase transformable ultrastable titanium-carboxylate framework for photoconduction. *Nat. Commun.* 9, 1660.
53. Serre, C., Groves, J.A., Lightfoot, P., Slawin, A.M.Z., Wright, P.A., Stock, N., Bein, T., Haouas, M., Taulelle, F., and Férey, G. (2006). Synthesis, structure and properties of related microporous N,N'-piperazinebismethylene phosphonates of aluminum and titanium. *Chem. Mater.* 18, 1451–1457.
54. Li, C., Xu, H., Gao, J., Du, W., Shangguan, L., Zhang, X., Lin, R., Wu, H., Zhou, W., Liu, X., et al. (2019). Tunable titanium metal-organic frameworks with infinite 1D Ti-O rods for efficient visible-light-driven photocatalytic H<sub>2</sub> evolution. *J. Mater. Chem. A* 7, 11928–11933.
55. Keum, Y., Park, S., Chen, Y.P., and Park, J. (2018). Titanium-carboxylate metal-organic framework based on an unprecedented Ti-oxo chain cluster. *Angew. Chem. Int. Ed. Engl.* 57, 14852–14856.
56. Yuan, S., Liu, T.-F., Feng, D., Tian, J., Wang, K., Qin, J., Zhang, Q., Chen, Y.P., Bosch, M., Zou, L., et al. (2015). A single crystalline porphyrinic titanium metal-organic framework. *Chem. Sci.* 6, 3926–3930.
57. Padial, N.M., Castells-Gil, J., Almora-Barrios, N., Romero-Angel, M., da Silva, I., Barawi, M., García-Sánchez, A., de la Peña O'Shea, V.A., and Martí-Gastaldo, C. (2019). Hydroxamate titanium-organic frameworks and the effect of siderophore-type linkers over their photocatalytic activity. *J. Am. Chem. Soc.* 141, 13124–13133.
58. Wang, S., Reinsch, H., Heymans, N., Wahiduzzaman, M., Martineau-Corcos, C., De Weireld, G., Maurin, G., and Serre, C. (2020). Toward a rational design of titanium metal-organic frameworks. *Matter* 2, 440–450.
59. Hendon, C.H., Tiana, D., Fontecave, M., Sanchez, C., D'arras, L., Sassoye, C., Rozes, L., Mellot-Draznieks, C., and Walsh, A. (2013). Engineering the optical response of the titanium-MIL-125 metal-organic framework through ligand functionalization. *J. Am. Chem. Soc.* 135, 10942–10945.
60. Fu, Y., Sun, D., Chen, Y., Huang, R., Ding, Z., Fu, X., and Li, Z. (2012). An amine-functionalized titanium metal-organic framework photocatalyst with visible-light-induced activity for CO<sub>2</sub> reduction. *Angew. Chem. Int. Ed. Engl.* 51, 3364–3367.
61. Duran, D., Couster, S.L., Desjardins, K., Delmotte, A., Fox, G., Meijers, R., Moreno, T., Savko, M., and Shepard, W. (2013). PROXIMA 2A – a new fully tunable micro-focus beamline for macromolecular crystallography. *J. Phys. Conf. Ser.* 425, 012005.
62. Reinsch, H., van der Veen, M.A., Gil, B., Marszalek, B., Verbiest, T., de Vos, D., and Stock, N. (2013). Structures, sorption characteristics, and nonlinear optical properties of a new series of highly stable aluminum MOFs. *Chem. Mater.* 25, 17–26.
63. Férey, G., and Serre, C. (2009). Large breathing effects in three-dimensional porous hybrid matter: facts, analyses, rules and consequences. *Chem. Soc. Rev.* 38, 1380–1399.
64. Férey, G. (2016). Giant flexibility of crystallized organic-inorganic porous solids: facts, reasons, effects and applications. *New J. Chem.* 40, 3950–3967.
65. Leshuk, T., Parviz, R., Everett, P., Krishnakumar, H., Varin, R.A., and Gu, F. (2013). Photocatalytic activity of hydrogenated TiO<sub>2</sub>. *ACS Appl. Mater. Interfaces* 5, 1892–1895.
66. Chen, X., Liu, L., and Huang, F. (2015). Black titanium dioxide (TiO<sub>2</sub>) nanomaterials. *Chem. Soc. Rev.* 44, 1861–1885.
67. Liu, L., and Chen, X. (2014). Titanium dioxide nanomaterials: self-structural modifications. *Chem. Rev.* 114, 9890–9918.
68. Reinsch, H., Waitschat, S., and Stock, N. (2013). Mixed-linker MOFs with CAU-10 structure: synthesis and gas sorption characteristics. *Dalton Trans.* 42, 4840–4847.
69. Deng, H., Doonan, C.J., Furukawa, H., Ferreira, R.B., Towne, J., Knobler, C.B., Wang, B., and Yaghi, O.M. (2010). Multiple functional groups of varying ratios in metal-organic frameworks. *Science* 327, 846–850.
70. Foo, M.L., Matsuda, R., and Kitagawa, S. (2014). Functional hybrid porous coordination polymers. *Chem. Mater.* 26, 310–322.
71. Helal, A., Yamani, Z.H., Cordova, K.E., and Yaghi, O.M. (2017). Multivariate metal-organic frameworks. *Natl. Sci. Rev.* 4, 296–298.

72. Ding, M., Flraig, R.W., Jiang, H.L., and Yaghi, O.M. (2019). Carbon capture and conversion using metal-organic frameworks and MOF-based materials. *Chem. Soc. Rev.* 48, 2783–2828.
73. Li, R., Hu, J., Deng, M., Wang, H., Wang, X., Hu, Y., Jiang, H.L., Jiang, J., Zhang, Q., Xie, Y., and Xiong, Y. (2014). Integration of an inorganic semiconductor with a metal-organic framework: a platform for enhanced gaseous photocatalytic reactions. *Adv. Mater.* 26, 4783–4788.
74. Cabrero-Antonino, M., Remiro-Buenamañana, S., Souto, M., García-Valdivia, A.A., Choquesillo-Lazarte, D., Navalón, S., Rodríguez-Díezquez, A., Mínguez Espallargas, G., and García, H. (2019). Design of cost-efficient and photocatalytically active Zn-based MOFs decorated with Cu<sub>2</sub>O nanoparticles for CO<sub>2</sub> methanation. *Chem. Commun.* 55, 10932–10935.
75. Ulmer, U., Dingle, T., Duchesne, P.N., Morris, R.H., Tavasoli, A., Wood, T., and Ozin, G.A. (2019). Fundamentals and applications of photocatalytic CO<sub>2</sub> methanation. *Nat. Commun.* 10, 3169.
76. Younas, M., Loong Kong, L.L., Bashir, M.J.K., Nadeem, H., Shehzad, A., and Sethupathi, S. (2016). Recent advancements, fundamental challenges, and opportunities in catalytic methanation of CO<sub>2</sub>. *Energ. Fuels* 30, 8815–8831.
77. Mateo, D., Albero, J., and García, H. (2019). Titanium-perovskite-supported RuO<sub>2</sub> nanoparticles for photocatalytic CO<sub>2</sub> methanation. *Joule* 3, 1949–1962.
78. Wenderich, K., and Mul, G. (2016). Methods, mechanism, and applications of photodeposition in photocatalysis: a review. *Chem. Rev.* 116, 14587–14619.
79. Giang, T.P.L., Tran, T.N.M., and Le, X.T. (2012). Preparation and characterization of titanium dioxide nanotube array supported hydrated ruthenium oxide catalysts. *Adv. Nat. Sci. Nanosci. Nanotechnol.* 3, 015008.
80. Morgan, D.J. (2015). Resolving ruthenium: XPS studies of common ruthenium materials. *Surf. Interface Anal.* 47, 1072–1079.
81. Albero, J., Peng, Y., and García, H. (2020). Photocatalytic CO<sub>2</sub> reduction to C<sub>2</sub>+products. *ACS Catal.* 10, 5734–5749.
82. Mateo, D., Santiago-Portillo, A., Albero, J., Navalón, S., Alvaro, M., and García, H. (2019). Long-term photostability in terephthalate metal-organic frameworks. *Angew. Chem. Int. Ed. Engl.* 58, 17843–17848.
83. Mateo, D., Albero, J., and García, H. (2018). Graphene supported NiO/Ni nanoparticles as efficient photocatalyst for gas phase CO<sub>2</sub> reduction with hydrogen. *Appl. Catal. B* 224, 563–571.
84. Mateo, D., Albero, J., and García, H. (2017). Photoassisted methanation using Cu<sub>2</sub>O nanoparticles supported on graphene as a photocatalyst. *Energy Environ. Sci.* 10, 2392–2400.
85. Mateo, D., Asiri, A.M., Albero, J., and García, H. (2018). The mechanism of photocatalytic CO<sub>2</sub> reduction by graphene-supported Cu<sub>2</sub>O probed by sacrificial electron donors. *Photochem. Photobiol. Sci.* 17, 829–834.
86. Karthik, R., Govindasamy, M., Chen, S.M., Mani, V., Umamaheswari, R., and Balamurugan, T.S.T. (2016). Electrochemical study of nitrobenzene reduction using potentiostatic preparation of nephrolepis leaf like silver microstructure. *Int. J. Electrochem. Sci.* 11, 6164–6172.
87. Li, X., Yu, J., Jaroniec, M., and Chen, X. (2019). Cocatalysts for selective photoreduction of CO<sub>2</sub> into solar fuels. *Chem. Rev.* 119, 3962–4179.